JOURNAL OF SPACECRAFT AND ROCKETS
Vol. 36, No. 2, March–April 1999

Reynolds Number Effects on Low-Speed Aerodynamics of a Hypersonic Configuration

G. Neuwerth,* U. Peiter,† F. Decker,† and D. Jacob‡
Technical University of Aachen, 52062 Aachen, Germany

A Collaborative Research Center project is focused on fundamental design aspects of a hypersonic research configuration that consists of a lifting body with a delta planform of aspect ratio 1.1 and rounded leading edges. The aerodynamics of the configuration at Mach numbers below 0.3 are described. The conclusions are based on tests in different subsonic wind tunnels. Pressure distribution measurements were carried out at a Reynolds number range of $3 \times 10^6 \le Re \le 40 \times 10^6$ using different wind-tunnel models. Above an angle of attack of 8 deg, the flow at the suction side changes and a concentrated vortex system (primary and secondary vortices) begins to form, causing local pressure minima in the pressure distribution. On rounded leading edges, the primary separation line is not a priori fixed and the vortex system has less intensity than for delta wings with sharp leading edges. The present investigations show that, in this case, the location of the separation line and the strength and location of the vortex system depend on the Reynolds number. Pressure distribution measurements at higher Reynolds numbers with a large model in the German–Dutch Wind Tunnel supported these observations. In particular, the high spatial resolution allowed a good physical interpretation of the flowfield. Knowledge of the flow processes was improved by surface oil-flow patterns, the laser-light-sheet technique, and particle image velocimetry.

Nomenclature

C_p	= pressure coefficient
l_i	= center chord length
M	= Mach number
Re	= Reynolds number, $l_i \cdot V_\infty / \nu$
Re_{local}	= local Reynolds number, $x \cdot V_\infty / \nu$
s_{local}	= local half-span
V	= flow velocities in the y-z plane
V_∞	= freestream velocity
x, y, z	= coordinates (see Fig. 1)
α	= angle of attack
ν	= viscosity
ω_x	= x component of vorticity

Introduction

THE Collaborative Research Center SFB 253 “Fundamentals of Design of Aerospace Planes” at the Technical University (RWTH) Aachen is focused on the basic design aspects of a hypersonic research configuration called Elliptical Aerodynamic Configuration (ELAC)-1. The project, which started in July 1989, includes theoretical and experimental research on a broad range of aerodynamic, propulsion, and structural subjects. ELAC-1 represents the lower stage of a two-stage space transportation system that takes off and lands horizontally. It is a lifting body with a delta planform of aspect ratio 1.1 and rounded leading edges. Figure 1 shows the geometry and the overall dimensions of this configuration. The cross sections consist of two half-ellipses with an axis ratio of 1:4 for the upper part and a ratio of 1:6 for the lower part. The elliptical cross sections lead to large radii at the leading edges of the delta wing. The air-breathing propulsion system will be integrated at the underside of ELAC-1. The forepart of the lifting body serves as an inlet and a compression region. The rear part is used as an expansion ramp. Two stabilizer fins profiled with NACA 0010 are used to control the vehicle. Their dihedral angle is 65 deg.

The low-speed aerodynamics of this configuration, especially during takeoff and landing, are described. At higher angles of attack, the flowfield around such a configuration is dominated by a vortex system on the suction side. The formation of the vortex system is closely related to flow separation at the rounded leading edges. The flow around a sharp-nosed delta wing separates directly at the leading edge so that the location of the separation line is known in advance. Numerical methods for calculating the flowfields around sharp-edged delta wings are based on this a priori knowledge. For a rounded leading edge, the exact position of the primary separation line is not known. It will be shown in this paper that their position is strongly influenced by the Reynolds number.

There are numerous papers dealing with the low-speed aerodynamics of sharp-edged delta wings, e.g., Refs. 1–8, which report force, moment, pressure, and flowfield measurements. One result is that the overall forces and moments for these wings are nearly independent of the Reynolds number because of the fixed primary separation lines. Only a few papers address the influence of leading-edge geometry, although this is of considerable importance because reusable space planes have rounded leading edges. References 9–12 show that the nonlinear vortex lift for rounded leading edges is smaller than for sharp ones and the formation of the vortex system starts at higher angles of attack. These effects depend on local and global Reynolds numbers. This paper, which deals with the aerodynamics of such a hypersonic configuration at subsonic speeds in a wide range of Reynolds numbers, contributes new results to explain these effects.

Wind-Tunnel Models

Within the framework of this project, 17 models of the configuration ELAC were built and tested in six different low-speed wind tunnels. These are the subsonic wind tunnels of the Universities in Aachen and Darmstadt, the Low-Speed Wind Tunnel Braunschweig of the German Aerospace Research Center (DLR) Braunschweig, the High-Pressure Wind Tunnel Göttingen (HDG) of the DLR Göttingen, the Kryo Wind Tunnel Cologne (KKK) of the DLR Cologne, and the German–Dutch Wind Tunnel (DNW) in Emmeloord, The Netherlands. In all tunnels the Mach number M was smaller than 0.3. The length scales of the models were 1:240, 1:65, and 1:12, with Reynolds numbers based on the center chord length l_i in the range of $3 \times 10^6 \le Re \le 40 \times 10^6$. The higher Reynolds numbers became possible in the HDG because of high pressures in the test

---

Presented as Paper 98-1578 at the AIAA 8th International Space Planes and Hypersonic Systems and Technologies Conference, Norfolk, VA, April 27–30, 1998; received May 7, 1998; revision received Aug. 17, 1998; accepted for publication Aug. 23, 1998.

*Senior Research Engineer, Institute of Aeronautics and Astronautics, Wüllnerstrasse 7.

†Research Engineer, Institute of Aeronautics and Astronautics, Wüllnerstrasse 7.

‡Professor and Head of Institute, Institute of Aeronautics and Astronautics, Wüllnerstrasse 7. Member AIAA.

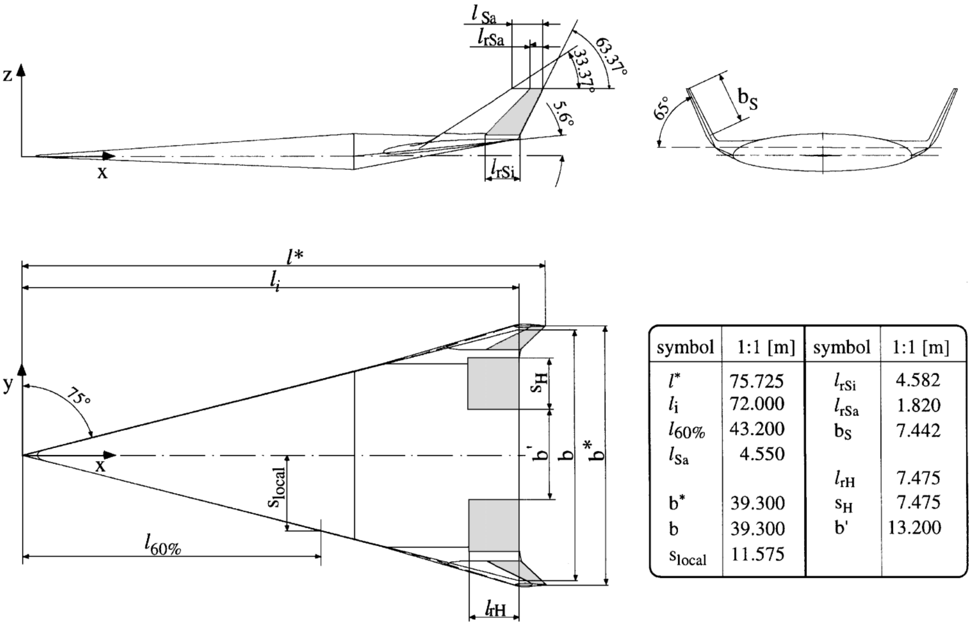

symbol	1:1 [m]	symbol	1:1 [m]
l^*	75.725	l_{rSi}	4.582
l_i	72.000	l_{rSa}	1.820
$l_{60\%}$	43.200	b_S	7.442
l_{Sa}	4.550		
		l_{rH}	7.475
b^*	39.300	s_H	7.475
b	39.300	b'	13.200
s_{local}	11.575		

Fig. 1 Geometry of the hypersonic research configuration ELAC-1.

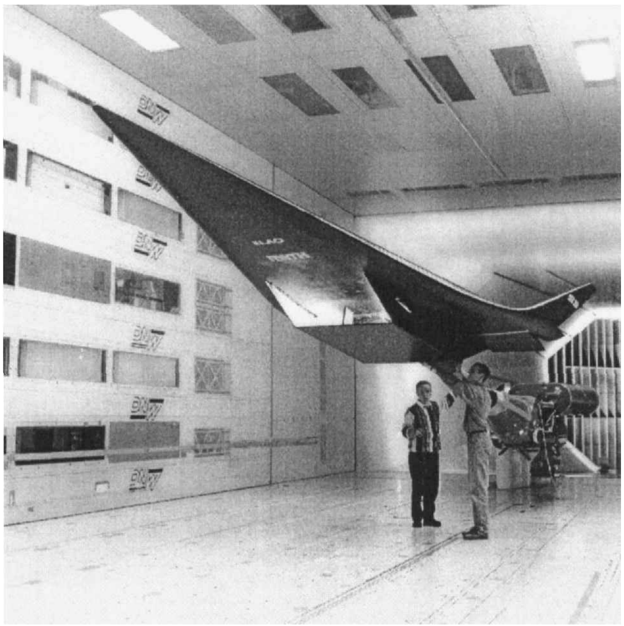

Fig. 2 ELAC-1 in the DNW test section.

section, in the KKK because of low temperatures, and in the DNW because of a larger length scale. The 1:12 scale model for the DNW had a $l_i = 6$ m, a reference wing area of nearly 10 m^2, and a mass of about 1600 kg. It was designed by the Institute of Aeronautics and Astronautics (ILR) at the RWTH Aachen. The strength and the stiffness of the load-bearing structure were computed by the Institute of Aerospace Structures at the RWTH Aachen. Figure 2 shows this model in the closed 8×6 m^2 test section of the DNW. The model has an internal six-component strain-gauge balance and is mounted on a rear sting. Flaps and rudders are movable.

Pressure Distribution Measurements

Measurements of the steady pressures at the surface of ELAC-1 were conducted in different wind tunnels using different models. The pressure coefficients C_p were measured in four sections, as shown in Fig. 3 for the DNW model, which permitted a smaller spacing of the pressure tubes than with the smaller models. In the DNW the best accuracy for C_p measurements could be reached; including the measurement of the dynamic pressures, this accuracy was 1.2%. In Fig. 4 from Ref. 13, the pressure distribution for a smaller ELAC-1 model (length scale 1:65) is given for $Re = 3.7 \times 10^6$ at the cross section $x/l_i = 0.6$. The pressure coefficients C_p (accuracy of the measurements about 1.5%) are plotted for the left half cross section. At the suction side the C_p values are negative and show the typical behavior of a delta wing. For angles of attack higher than $\alpha = 8$ deg, a primary separation takes place at the leading edge ($y/s_{\mathrm{local}} = 1$). The free shear layer rolls up to the primary vortex, which induces additional velocities. These are directed outward and reach a maximum below the vortex axis. At that position on the surface, a clear pressure minimum results (Fig. 4). A laser-light-sheet picture (Fig. 5) shows this primary vortex in a cross section at $x/l_i = 0.6$ of the ELAC model. Looking from behind in the upstream direction, the shear layer can be seen separating at the leading edge and rolling up to a vortex. The strong pressure minima in Fig. 4 correspond to the position of the primary vortex axis. The increase in the surface pressure toward the leading edge leads to the secondary separation of the outward-directed flow. A secondary vortex develops, which also can be identified in Fig. 4, by a second and weaker minimum of the pressure distribution at $y/s_{\mathrm{local}} \approx 0.85$. The topology of this vortex system is outlined in Fig. 6.

With increasing α values, the circulation in the vortices increases and the low pressures at the surface are more pronounced, as Fig. 4 shows. The primary vortex is shifted toward the plane of symmetry of the wing.

In Fig. 7, the pressure distribution of ELAC-1 at $\alpha = 20$ deg is compared with measurements of Ref. 14 using a sharp-edged delta wing with an aspect ratio of 1 and a very similar angle of attack $\alpha = 20.5$ deg. Both pressure distributions are measured in a cross section at $x/l_i = 0.3$. The low pressures for the sharp-edged delta wing are stronger than for ELAC-1. The axes of the primary vortices for thick delta wings are located closer to the wing surface than for thin wings.[15] Because of the weaker pressure peak of ELAC-1, it follows that the vortex strength of delta wings with rounded leading edges is lower. Corresponding conclusions are made in Ref. 10, where it is pointed out that the nonlinear vortex lift is significantly higher for sharp-edged delta wings.

Figure 8 shows an oil-flow pattern that corresponds to the flow condition of Fig. 4 and $\alpha = 20$ deg. The primary separation line of the flow directly at the leading edge cannot be seen, but the outward (to the leading edge) directed flow induced by the primary vortex is shown clearly. Because the pressure is increasing along these streamlines, a secondary separation occurs. This separation

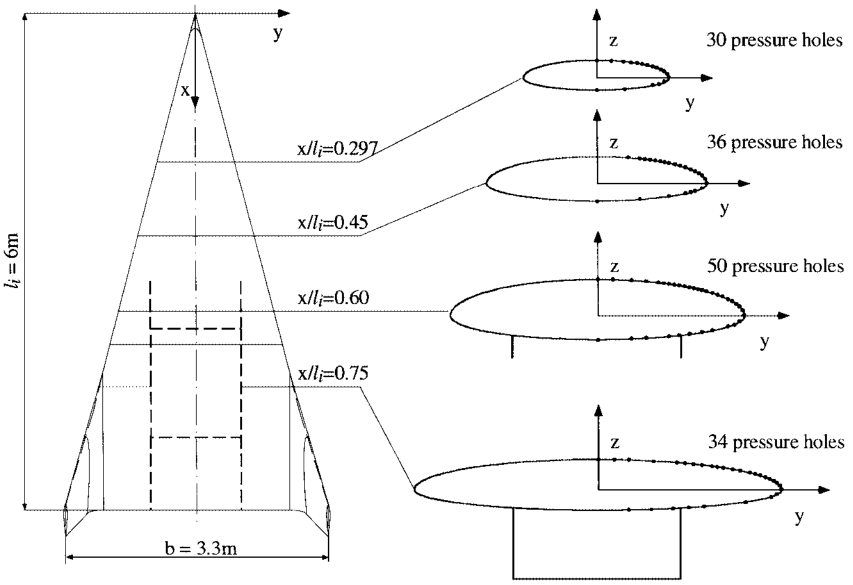

Fig. 3 Position of pressure holes for the DNW model.

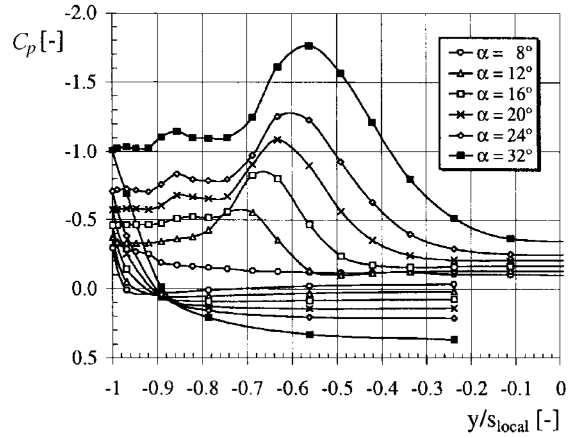

Fig. 4 Pressure distribution of the left of the cross section (x/l_i = 0.6, *Re* = 3.7 × 10^6).

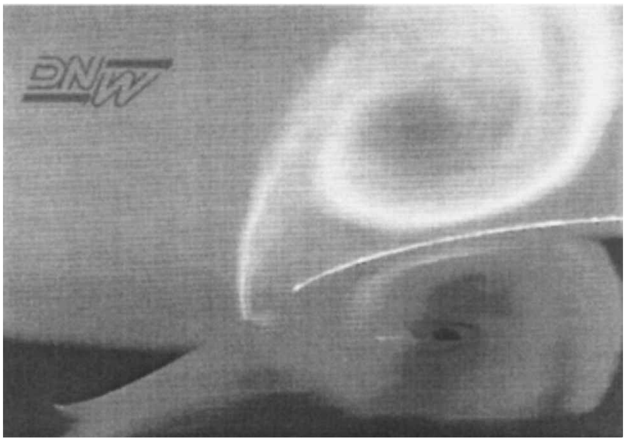

Fig. 5 Laser-light-sheet picture (x/l_i = 0.6, *Re* = 6.2 × 10^6, α = 21.58 deg).

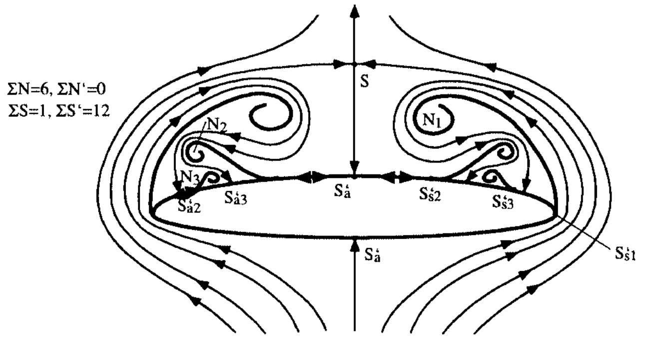

Fig. 6 Topology of vortex system for high angles of attack.

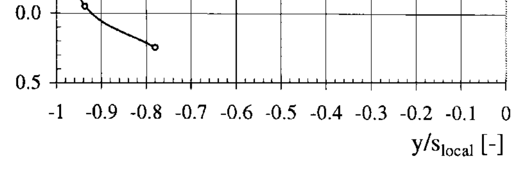

Fig. 7 Comparison of the pressure distributions (x/l_i = 0.3).

is marked as line 2 in Fig. 8. In the topological drawing (Fig. 6), this is marked as line S'_{s2}. The secondary vortex is formed and induces a flow away from the leading edge. In combination with the pressure distribution in this region, a tertiary vortex is developed in this case. The corresponding tertiary separation is marked as line 3 in Fig. 8 and as line S'_{s3} in Fig. 6. In the pressure distribution of Fig. 4, this tertiary vortex cannot be seen because this vortex is too weak.

Reynolds Number Variations Influencing Pressure Distributions

The condition of the boundary layer and the position of the transition from laminar to turbulent flow is very important for the strength and the position of the vortex system on the suction side. Investigations using liquid crystals (LC) have been conducted to get an overall picture of the boundary conditions.[13] The LCs, which are sensitive to temperature differences, make it possible to detect laminar and turbulent regions. The LC investigations in Ref. 13 were conducted in the subsonic wind tunnel of the ILR ($M \leq 0.3$) up to the maximum Reynolds number $Re = 4.9 \times 10^6$. They have shown that a small area near the leading edges on the suction side has a laminar boundary layer. All of the other regions on the suction side

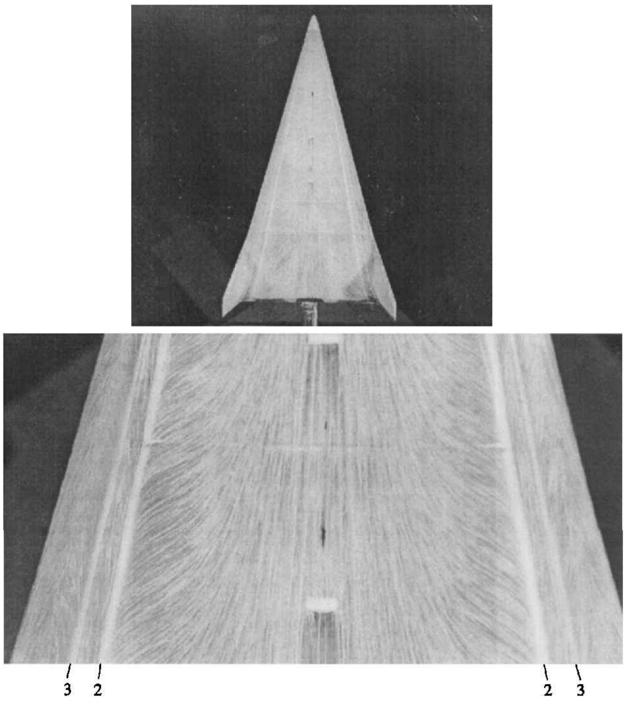

Fig. 8 Oil-flow pattern (Re = 3.7 × 10^6, α = 20 deg).

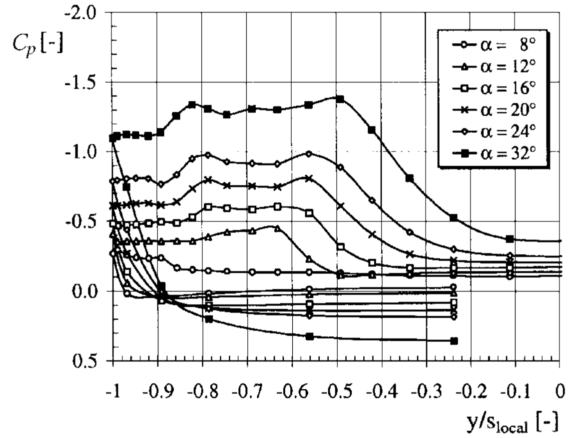

Fig. 9 Pressure distributions for laminar secondary separation (x/l_i = 0.6, Re = 1.1 × 10^6).

have turbulent boundary layers. The entire underside has laminar boundary layers. With increasing Reynolds numbers, the transition lines on the suction side move closer to the leading edges. It can be concluded that the boundary layer at the primary separation near the leading edge is laminar for all Reynolds numbers tested in the wind tunnel of the ILR. The secondary separation can take place in a turbulent or laminar region. These differences lead to strong variations in the pressure distributions. Figure 4 ($Re = 3.7 \times 10^6$) shows, for turbulent secondary separation, strong peaks caused by the primary vortex and relatively weak ones caused by the secondary vortex. The turbulent boundary layer in this case is able to resist for a longer distance the increasing pressure in the direction to the leading edge. The separation takes place relatively late, and a weak secondary vortex originates. If the boundary layer is laminar, the secondary separation occurs earlier, causing a bigger secondary vortex at a greater distance from the leading edge. The corresponding pressure distributions for this case ($Re = 1.1 \times 10^6$) are plotted in Fig. 9. Now the primary and secondary vortices are generating pressure peaks with nearly the same strength. This behavior is typical for laminar secondary separation. Because of the displacement of the enlarged secondary vortex, the primary vortex is moved inboard and away from the surface. The latter effect causes the reduction of the pressure peak of the primary vortex shown in Fig. 9.

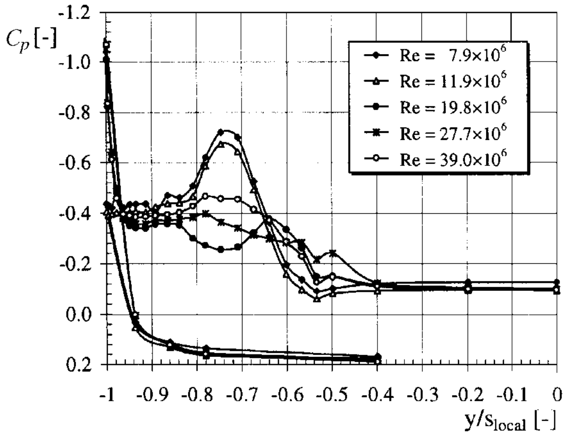

Fig. 10 Influence of Reynolds number on pressure distribution (x/l_i = 0.3, α = 12 deg).

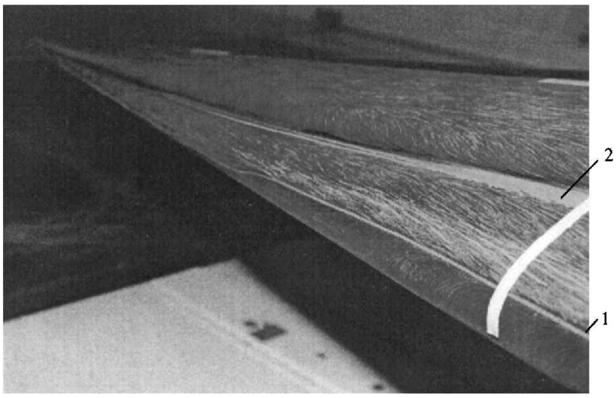

Fig. 11 Surface oil-flow pattern (Re = 19.8 × 10^6, α = 12 deg).

In the Reynolds number range up to $Re = 4.9 \times 10^6$, which was obtainable with the 1:65 ELAC-1 model, the primary separation line was always located at the leading edge. The 1:12 model in the DNW permitted investigations in a high-Reynolds-number range up to $Re = 39 \times 10^6$ combined with pressure distribution measurements having a sufficiently high spatial resolution. The high number of pressure holes, especially in the important region of the rounded leading edges, can be seen in Fig. 3.

Figure 10 shows pressure distributions for the DNW model in the cross section $x/l_i = 0.3$ for four different Reynolds numbers at $\alpha = 12$ deg. For the two lower Reynolds numbers $Re = 7.9 \times 10^6$ and $Re = 11.9 \times 10^6$, the primary separation occurs directly at the leading edge ($y/s_{\text{local}} = 1$) and leads to the well-known strong primary vortex ($C_p \approx -0.7$) at $y/s_{\text{local}} \approx 0.74$. However, for the three higher Reynolds numbers, a new phenomenon occurs. The flow does not separate at the leading edge, and therefore a strong suction peak arises at $y/s_{\text{local}} = 1$. The primary separation line is located on the upper side now. The shift of the separation line causes weaker primary vortices ($C_p \leq -0.48$). For $Re = 19.8 \times 10^6$ the separation lines are made visible in the surface oil-flow pattern of Fig. 11. Shown is the left-hand side of the model with a flow direction from the left to the right. The white tape marks the cross section $x/l_i = 0.3$. The primary separation, marked as line 1, is about 6 cm away from the leading edge on the suction side. The secondary separation, marked as line 2, is also clearly visible in Fig. 11. The suction peaks of the secondary vortex are hardly visible in Fig. 10. This behavior was expected because the boundary layer on the upper side of the ELAC-1 model in the regions of secondary separations for the Reynolds numbers of Fig. 10 is highly turbulent and leads to secondary vortices with less circulation.

It can be concluded that, with increasing Reynolds numbers, the primary separation line moves from the leading edge to the suction side of the model. This process starts in the rear part of ELAC-1 and moves to the front with increasing Reynolds numbers, as can be seen in Fig. 11. In the front part of the model, the primary separation line moves directly to the leading edge at about $x/l_i \approx 0.15$. This process is caused by a decrease in the local Reynolds number when the position x is decreased.

The boundary-layer transition on the suction side of the DNW model was investigated by the RWTH Aachen Institute of Aerodynamics using multisensor hot-film foils. Their time-dependent signals give information about the boundary-layer state. From the pressure distribution shown in Fig. 10, it can be deduced that the boundary layer at the leading edge is laminar for the two smaller Reynolds numbers $Re = 7.9 \times 10^6$ and 11.9×10^6. The boundary layers on the lower side of the model stay laminar for all Reynolds numbers tested because the flow is accelerated there due to the strong negative pressure gradients. The transition to a turbulent boundary layer occurs just above the leading edge. The signals of the multisensor hot-film foils show that the suction side has turbulent boundary layers for the relevant higher angles of attack. The LC investigations already have shown that, with increasing Reynolds numbers, the laminar regions become smaller and the transition lines move to the leading edges. For Reynolds numbers $Re = 19.8 \times 10^6$ and higher (see Fig. 10) the boundary layer must become turbulent at the lower side before reaching the leading edge. Therefore, the primary separation is delayed and the flow can follow the rounded leading edge for a while in spite of the strong increasing pressures at the upper side.

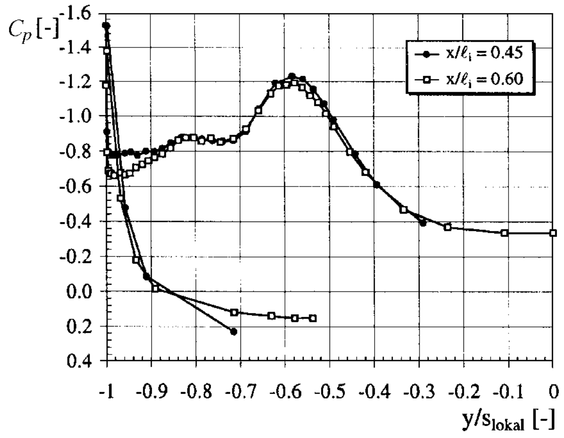

Fig. 12 Pressure distributions for the same local Reynolds number, $Re_{\text{local}} = 5 \times 10^6$, at different cross sections ($\alpha = 21$ deg).

In Fig. 12, two pressure distribution measurements in the cross sections $x/l_i = 0.45$ and 0.6 at $\alpha = 21$ deg are compared. In both cases the local Reynolds number based on the local x (distance of the cross section from the top) is about $Re_{\text{local}} = 5 \times 10^6$. It can be seen that the pressure distributions in Fig. 12 agree well. The spanwise positions and the suction peaks of the primary and secondary vortices, in particular, are very similar. Also, the pressures due to the delayed primary flow separation at the leading edge show a good agreement.

Application of Particle Image Velocimetry

Particle image velocimetry (PIV) permits one to capture the flow velocity of large flowfields instantaneously. This important feature of PIV makes it possible to measure the flowfield data of the complete, more or less unsteady vortex system in a cross section at the same time. The PIV measurements in the DNW were conducted by the Institute of Fluid Mechanics, DLR Göttingen. Four pulsed lasers generated a light sheet on the suction side of ELAC-1 in the cross section at $x/l_i = 0.6$. Two light pulses (duration 6 ns) were generated, each with an energy of 640 mJ. The separation time between these two pulses had to be chosen between 15 and 100 μs as a function of V_∞. Tiny special tracer particles in the flow are lit with the pulses and recorded with charge-coupled device (CCD) cameras (resolution 1008 × 1018 pixels). By analyzing the dislocation of the particles between the two light pulses, the velocity distribution can be computed. In this case, a two-dimensional PIV was used. This means that the radial and circumferential components of the vortex flowfields can be measured and analyzed. Two CCD cameras had to be installed to cover a sufficiently large part of the cross section. Figure 13 shows a two-dimensional vector plot of the velocity distribution computed from the PIV data with the parameters $x/l_i = 0.6$, $\alpha = 21$ deg, and $Re = 5.9 \times 10^6$. The separate areas observed by the two cameras can be seen. One camera was centered to the position of the primary vortex at 66% of the local semispan and $z/s_{\text{local}} = 0.44$. The second camera observed the shear-layer region emerging from the leading edge and the secondary vortex. In Fig. 13, average values of the velocities (from 40 instantaneous flowfield measurements), which are computed from 40 PIV measurements in quick succession ($f = 5$ Hz), are plotted. The highest values of the circumferential velocity induced by the primary vortex are $V_{\max} = 21$ m/s for $V_\infty = 15$ m/s. Figure 13 shows that the secondary vortex is weak and that it is situated at about 87% of the local

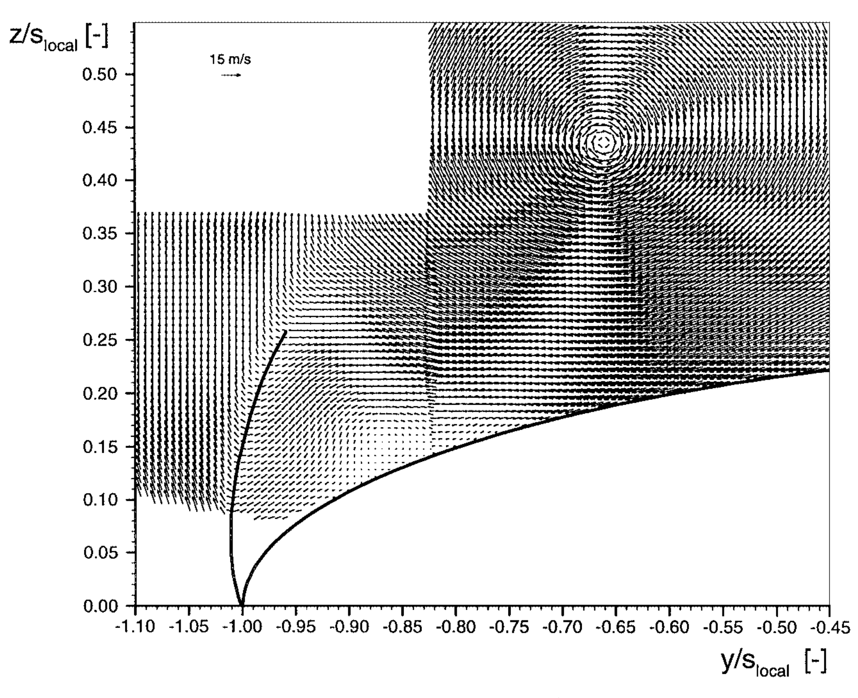

Fig. 13 Two-dimensional velocity field computed from PIV data ($x/l_i = 0.6$, $\alpha = 21$ deg, $Re = 5.9 \times 10^6$).

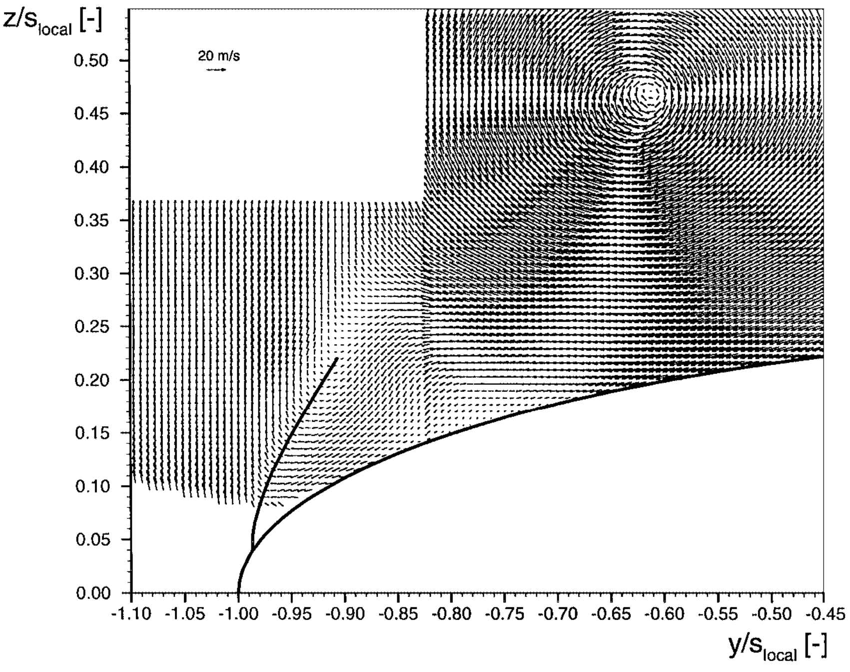

Fig. 14 Two-dimensional velocity field computed from PIV data ($x/l_i = 0.6$, $\alpha = 21$ deg, $Re = 7.8 \times 10^6$).

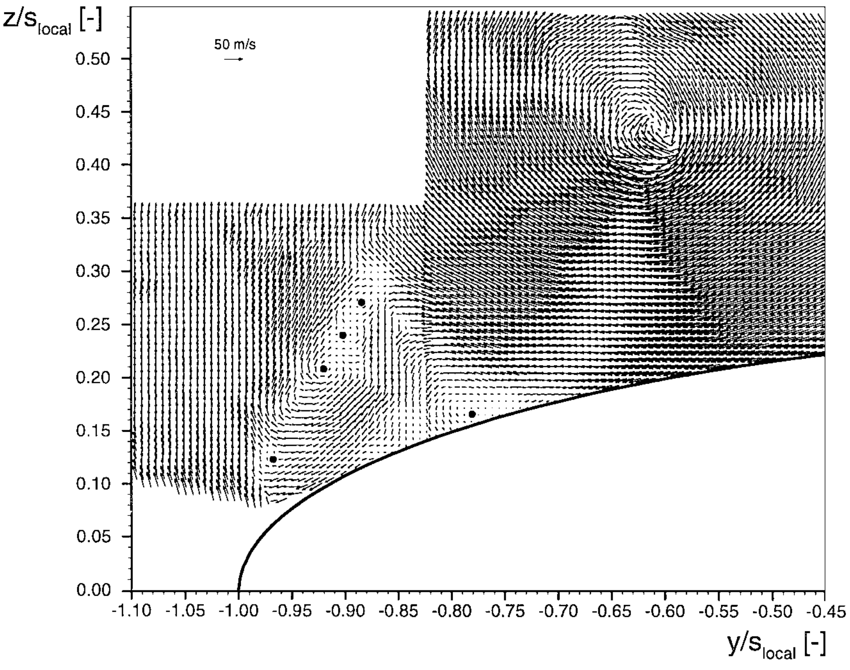

Fig. 15 Instantaneous flowfield computed from PIV data ($x/l_i = 0.6$, $\alpha = 21$ deg, $Re = 19.8 \times 10^6$).

semispan. It was not possible to observe the region at the leading edge from the position of the CCD cameras mounted downstream of the model because the cameras had to be mounted high above the model with a disadvantageous oblique orientation relative to the model. However, an extrapolation of the curved shear-layer position in Fig. 13 leads just to the leading edge.

For an increased Reynolds number $Re = 7.8 \times 10^6$, the PIV data result in the velocity field shown in Fig. 14. An extrapolation of the curved shear-layer position leads now to a position of the primary separation away from the leading edge on the suction side at about $z/s_{\text{local}} = 0.04$. This behavior corresponds to the pressure distribution in Fig. 12 ($x/l_i = 0.6$). A comparison with Fig. 13 shows that the primary vortex has moved inboard for about 5% of the local semispan. The pressure minimum in Fig. 12 due to the primary vortex is located at 63% of the local semispan. At this position the highest values of the velocities induced by the primary vortex are measured on the surface.

Figure 15 shows the instantaneous flowfield without time averaging. The parameters are identical to those of Fig. 14, but the Reynolds number is increased to $Re = 19.8 \times 10^6$. Comparing some of the 40 instantaneous PIV flowfield measurements shows that the location of the primary vortex axis is fluctuating with an amplitude of about ±0.5% of the local semispan (±50 mm). Figure 15 also shows that the flow near the vortex center at that moment is not symmetrical. The counter-rotating secondary vortex can be seen clearly at $y/s_{\text{local}} = 0.78$. An interesting feature is that, along the shear layer, a series of local instantaneous small vortices can be observed. All of these vortices are collected and rolled up into the primary vortex.

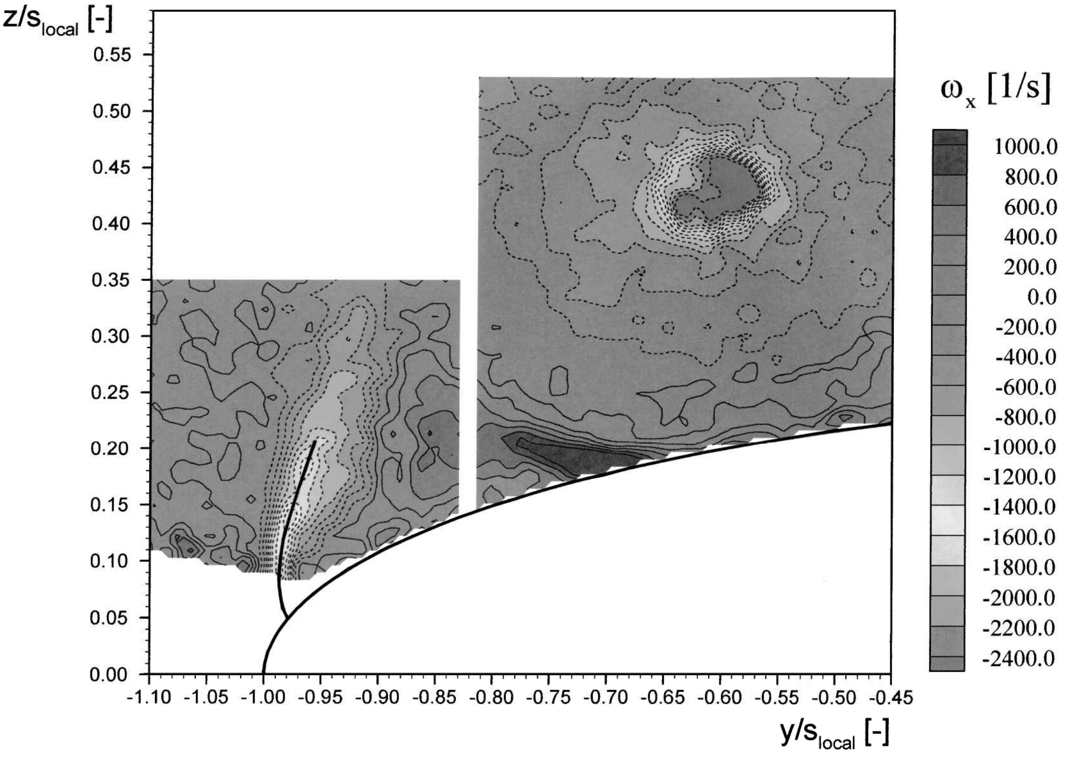

Fig. 16 Vorticity distribution ω_x computed from PIV data (parameters as in Fig. 15).

In Fig. 16, the vorticity distribution (ω_x component), which is computed from the average values of the velocities from 40 instantaneous PIV flowfield measurements, is plotted. The parameters are the same as in Fig. 15. The highly concentrated primary vortex is clearly visible with a high vorticity concentration ($\omega_x = -3110\ \mathrm{s}^{-1}$). Further high vorticity (also with negative sign) occurs in the region of the free shear layer starting at the primary separation line. A third region with increased vorticity (now with positive sign) is near the secondary separation line at about $y/s_{\mathrm{local}} = 0.7$.

Conclusions

The Collaborative Research Center SFB 253 at RWTH Aachen is focused on fundamental design aspects of a hypersonic research configuration called ELAC-1, a lifting body with a delta planform of aspect ratio 1.1 and rounded leading edges. The low-speed aerodynamics of ELAC-1 are described. Several differently scaled wind-tunnel models and measurements in six different subsonic wind tunnels lead to an extensive database.

The flowfield of a delta wing with such a low aspect ratio is dominated by a vortex system on the suction side. The investigations have shown that, for a delta wing with rounded leading edges, the location of the primary separation line and also the strength and location of the vortex system depend on the Reynolds number. For a sharp-edged delta wing, where the primary separation line is a priori fixed at the leading edge, the circulation of the vortex systems and the corresponding nonlinear lift force is much higher.

For Reynolds numbers up to $Re = 4.9 \times 10^6$ (referred to the center chord length of the model) the primary separation line is located always just at the leading edge. For higher Reynolds numbers, however, the primary separation line moves to the upper side of the delta wing. A strong suction peak at the leading edge arises, and the strength of the primary vortex is decreased. The secondary vortices are weak at the high Reynolds numbers because the secondary separation occurs now in a region with turbulent boundary layers. The pressure distributions in different cross sections agree well if the local Reynolds number is the same. The analysis of these processes was supported by surface oil-flow patterns, the laser-light-sheet technique, and PIV.

PIV makes it possible to measure the flowfield data of the complete, more or less unsteady vortex system in a cross section at the same time. An interesting feature is that, along the shear layer emerging from the primary separation line, a series of local instantaneous small vortices can be observed. All of these vortices are collected and rolled up into the primary vortex.

Acknowledgments

The German–Dutch Wind Tunnel is a large, versatile low-speed wind tunnel. For the first time a university had the opportunity to use this facility as a project coordinator and to investigate an aerospace plane extensively there. The authors thank the German Research Association for sponsoring these measurements, which improved the interpretation of the flow processes for delta wings with rounded leading edges. Further on, this project was supported by the German Aerospace Research Center (DLR). The DLR contributed the particle image velocimetry using a highly sophisticated measurement system.

References

[1] Fink, P. T., "Wind Tunnel Tests on a Slender Delta Wing at High Incidence," *Zeitschrift für Flugwissenschaften Weltraumforschung*, Vol. 4, No. 7, 1956, pp. 247–249.

[2] Marsden, D. J., Simpson, R. W., and Rainbird, W. J., "An Investigation into the Flow over Delta Wings at Low Speeds with Leading-Edge Separation," Cranfield College of Aeronautics, Rept. 114, 1959.

[3] Hummel, D., "Experimentelle Untersuchung der Strömung auf der Saugseite eines schlanken Deltaflügels," *Zeitschrift für Flugwissenschaften Weltraumforschung*, Vol. 13, No. 7, 1965, pp. 247–252.

[4] Hummel, D., "Zur Umströmung scharfkantiger schlanker Deltaflügel bei großen Anstellwinkeln," *Zeitschrift für Flugwissenschaften Weltraumforschung*, Vol. 15, No. 10, 1967, pp. 376–385.

[5] Lambourne, N. C., and Bryer, D. W., "The Bursting of Leading-Edge Vortices—Some Observations and Discussion of the Phenomenon," Aeronautical Research Council, Repts. and Memoranda No. 3282, Ministry of Aviation, London, 1962.

[6] Hummel, D., "Untersuchungen über das Aufplatzen der Wirbel an schlanken Deltaflügeln," *Zeitschrift für Flugwissenschaften Weltraumforschung*, Vol. 13, No. 5, 1965, pp. 158–168.

[7] Hummel, D., and Redeker, G., "Über den Einfluß des Aufplatzens der Wirbel auf die aerodynamischen Beiwerte von Deltaflügeln mit kleinem Seitenverhältnis beim Schiebeflug," *Jahrbuch der WGLR*, Oct. 1967, pp. 232–240.

[8] Hummel, D., "On the Vortex Formation over a Slender Wing at Large Angles of Incidence," *High Angles of Attack Aerodynamics*, CP-247, AGARD, 1978 (Paper 15).

[9] Bartlett, G. E., and Vidal, R. J., "Experimental Investigation of Influence of Edge Shape on the Aerodynamic Characteristics of Low Aspect Ratio Wings at Low Speeds," *Journal of the Aeronautical Sciences*, Vol. 22, No. 8, 1955, pp. 517–532.

[10] Gersten, K., and Hummel, D., "Untersuchungen über den Einfluß der Vorderkantenform auf die aerodynamischen Beiwerte schiebender Pfeil- und Deltaflügel von kleinem Seitenverhältnis," Deutsche Luft- und Raumfahrt, Forschungsbericht, No. 86, Inst. für Aerodynamik, Braunschweig, Germany, Dec. 1966.

[11] Truckenbrodt, E., and Feindt, E. G., "Untersuchungen über das Abreißverhalten von Deltaflügeln in inkompressibler Strömung," *Zeitschrift für Flugwissenschaften Weltraumforschung*, Vol. 6, No. 4, 1958, pp. 97–102.

[12] Hendersen, W. P., "Effects of Wing Leading-Edge Radius and Reynolds Number on Longitudinal Aerodynamic Characteristics of High Swept Wing-Body Configurations at Subsonic Speeds," NASA TN-D-8361, 1976.

[13] Decker, F., "Experimentelle und theoretische Untersuchungen zur Aerodynamik der Hyperschallkonfiguration ELAC-1 im Niedergeschwindigkeitsbereich," Ph.D. Dissertation, Inst. für Luft- und Raumfahrt, RWTH Aachen, Cuvillier Verlag, Göttingen, Germany, 1997.

[14] Hummel, D., and Redeker, G., "Experimentelle Bestimmung der gebundenen Wirbellinien sowie des Strömungsverlaufs in der Umgebung der Hinterkante eines schlanken Deltaflügels," *Abhandlungen der Braunschweigischen Wissenschaftlichen Gesellschaft*, Vol. 22, 1972, pp. 273–290.

[15] Staudacher, W., "Die Beeinflussung von Vorderkantenwirbelsystemen schlanker Tragflügel," Ph.D. Dissertation, Inst. für Aerodynamik und Gasdynamik, Univ. of Stuttgart, Stuttgart, Germany, 1992.

J. R. Maus
Associate Editor